

AIR-MASS TRANSFORMATION ACROSS THE SST FRONT IN THE KUROSHIO EXTENSION REGION RETRIEVED BY THE SURFACE FLUX BUOYS AND ADVANCED MICROWAVE SCANNING RADIOMETER FOR EARTH OBSERVATION SATELLITE

M. Konda

Department of Geophysics, Graduate School of Science, Kyoto University, Kitashirakawa-Oiwake, Sakyo, Kyoto, Kyoto 606-8502, Japan – konda@kugi.kyoto-u.ac.jp

KEY WORDS: Turbulent heat flux, Kuroshio Extension, SST front, Air-sea interaction, Air mass transformation, AMSR-E

ABSTRACT:

Wintertime sea surface heat flux variability across the Kuroshio Extension (KE) front is analyzed using two surface flux buoys moored on the northern and the southern sides of the KE front as well as the observation by Advanced Microwave Scanning Radiometer for Earth Observation Satellite (AMSR-E). The combined use of the wind speed and the other AMSR-E products (the sea surface temperature and the integrated water vapor) provides the instantaneous latent heat flux at every observation cells. The coincident data used are from periods during two winters in 2007 and 2008, when the two surface buoys had a complete suite of meteorological data. In these two winter periods, we focus on three types of typical weather patterns referred to here as: the northerly wind condition, the monsoon wind condition, and the normal condition. The difference in the surface heat flux between these conditions is attributed to the different air mass transformation. We analyzed the spatial change of the boundary layer parameters and their influence on the surface heat flux between the two buoys. During the northerly wind condition, the satellite measurement captures the rapid increase of the surface water vapor content associated with the SST front because of the nonlinearity of the Clausius-Clapeyron relation. It is found that the change is consistent with the large latent heat flux in spite of the weaker wind speed in the southern side of the SST front.

1. INTRODUCTION

The importance of measuring and monitoring the TBF is quite important in the region, where the heat flux is very large and therefore the air-sea interaction is very strong. The western boundary current region such as the Kuroshio Extension (KE) region is one of the key are for investigating the role of the thermal coupling between the ocean and the atmosphere.

Nakamura et al. (2008) and Nonaka et al. (2009) suggested from atmospheric general circulation model experiments that the strong restoring of the near-surface air temperature to the SST front affected the activity of the mid-latitude stormtracks through the adjustment of the turbulent surface heat flux. Although many surface heat flux data sets show that the area of the large latent heat flux (LHF) expands to both sides of the KE in cooling seasons (Kubota et al., 2003; Qiu et al. 2004), the boundary layer processes and the oceanic and meteorological parameters are likely to be quite different on either side of the KE. Such a discrepancy suggests a spatial difference of the ocean-atmosphere feedback system in the KE region.

Recently, Pacific Marine Environment Laboratory (PMEL)/ National Oceanic and Atmospheric Administration (NOAA) operates the Kuroshio Extension Observatory (KEO) buoy at 144.6°E, 32.4°N, while Japan Agency for Marine-Earth Science and Technology (JAMSTEC) does JAMSTEC KEO (JKEO) buoy at 146.5°E, 38.0°N. These buoys are measuring the surface meteorology and the underwater physical properties at the south and the north across the Kuroshio Extension (Cronin et al. 2008). The evaluating the air-sea coupling process by using these in situ measurements is very important for applying the satellite-derived heat flux to the air-sea interaction study.

Using the National Centers for Environmental Prediction-National Center for Atmospheric Research reanalysis product (Kalney et al., 1996) and the net air-sea heat flux at KEO as an index, Bond and Cronin (2008) extracted a composite SLP pattern associated with large heat flux at KEO that corresponded to a typical wintertime SLP weather pattern. In this study, we focus on the variations associated with three different typical wintertime weather conditions and discuss the implications for interannual climate variations.

The microwave radiometer has a merit of measuring together the other environmental parameters like water vapor content or sea surface temperature (SST). The instantaneous observation of these physical properties enables us to obtain information about phenomena in which they work together. Obtaining the snapshot turbulent heat flux (THF) should be the most attractive product of the combined use of physical variables obtained by Advanced Microwave Scanning Radiometer on Earth Observing System (AMSR-E) on Aqua, as it simultaneously measures the wind speed, SST, and integrated water vapor, and therefore the surface humidity. Spatial distribution of these parameters derived by AMSR-E and the LHF will give the information over the gap between these surface flux buoys.

2. DATA

In this study, the AMSR-E wind speed is retrieved from the measured BTs provided by Japan Aerospace Exploration Agency (JAXA) in a form of the AMSR-E level 1B data set, according to the method described in Konda et al.(2006).

NOAA / PMEL operates the KEO buoy at 144.6°E, 32.4°N to the south of the KE front, while JAMSTEC operates the JKEO buoy at 146.5°E, 38.0°N to the north of the front (Fig. 1). The

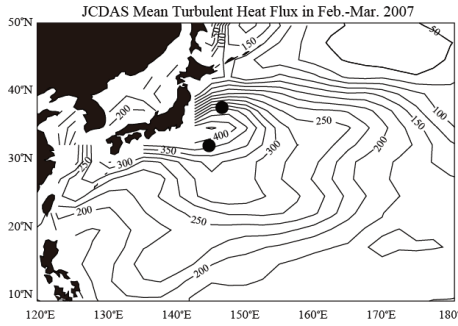


Figure 1: Mean turbulent heat flux in the northwest Pacific sector during Period I. The mean value is computed from JCDAS product. Positions of KEO (filled black circle: 144.6°E, 32.4°N) and JKEO (unfilled black circle: 146.5°E, 38.0°N) are superimposed. The 16°C isotherm is also superimposed by the thick broken line as a proxy of the SST front associated with the KE jet.

KEO buoy was first deployed on June 16, 2004, while the JKEO buoy was first deployed on 18 February 2007. For this study, we use data only from the first JKEO deployment period, which ended on 24 March 2008. The study period in which both KEO and JKEO had complete measurements thus spans portions of winters both in 2007 and 2008. These winter portions (Period I: 18 February to 12 March 2007 and Period II: 1 to 25 January 2008) will be considered separately.

Sensible heat flux (SHF) and LHF are computed from the high resolution data using the version 3.0 Coupled Ocean-Atmosphere Response Experiment (COARE) bulk algorithm (Fairall et al., 2003). As the focus of this study is to analyze the factors that produce a TBF difference between JKEO and KEO, we will decompose the bulk heat transfer equation into terms representing spatial anomalies of individual ABL parameters. The spatial anomaly of the TBF is defined in this study as the difference between JKEO and KEO as follows.

$$\begin{aligned}
 H' &= H^{JKEO} - H^{KEO} \\
 &= \rho C_p C_h^{JKEO} (T_s^{JKEO} - T_a^{JKEO}) U_a^{JKEO} - \rho C_p C_h^{KEO} (T_s^{KEO} - T_a^{KEO}) U_a^{KEO} \quad (i) \\
 &= \rho C_p C_h^{KEO} \{ (T_s' - T_a') U_a^{JKEO} \\
 &\quad + (T_s^{KEO} - T_a^{KEO}) U_a' \} \quad (ii) \\
 &\quad + \rho C_p C_h' (T_s^{KEO} - T_a^{KEO}) U_a^{JKEO} \quad (iii) \\
 &\quad + R_H \quad (iv)
 \end{aligned} \tag{2}$$

and,

$$\begin{aligned}
 Q' &= Q^{JKEO} - Q^{KEO} \\
 &= \ell \rho C_e^{JKEO} (q_s^{JKEO} - q_a^{JKEO}) U_a^{JKEO} - \ell \rho C_e^{KEO} (q_s^{KEO} - q_a^{KEO}) U_a^{KEO} \quad (i) \\
 &= \ell \rho C_e^{KEO} \{ (q_s' - q_a') U_a^{JKEO} \\
 &\quad + (q_s^{KEO} - q_a^{KEO}) U_a' \} \quad (ii) \\
 &\quad + \ell \rho C_e' (q_s^{KEO} - q_a^{KEO}) U_a^{JKEO} \quad (iii) \\
 &\quad + R_Q \quad (iv)
 \end{aligned} \tag{3}$$

where H and Q respectively indicate the SHF and the LHF, and T , q and U respectively denote temperature, specific humidity and wind speed with subscripts indicating values at sea surface (s) and at the height of meteorological sensors on the buoy hull (a). Superscripts indicate whether the value is at JKEO or KEO and the prime indicates the difference between them. Likewise,

ρ denotes the density of the atmosphere, C_p the specific heat at constant pressure and ℓ the latent heat of evaporation. C_h and C_e are respectively bulk transfer coefficients of heat and moisture, calculated from the COARE 3.0 model.

Term (i) is the heat flux difference between JKEO and KEO, and terms (ii) and (iii) respectively show the contributions of the spatial anomaly in air-sea gradients of temperature ($\Delta T'$) and humidity ($\Delta q'$) (where Δ represents the sea minus air difference), and that in wind speed (U_a'). Term (iv) represents the component caused by the spatial variation of the bulk transfer coefficients C_h' and C_e' . R_H and R_Q respectively indicate the terms of higher degree of spatial anomalies.

After analyzing the spatial differences between KEO and JKEO, the regional patterns in the TBF will be considered using flux product of the Japan Meteorological Agency Climate Data Assimilation System (JCDAS) from the Japanese 25-year Reanalysis Project (JRA25) (Onogi et al. 2007). The TBF averaged during the two cold periods in the KE region are shown in Fig. 1.

3. RESULTS

Temporal variability of the SHF and the LHF during Period I and II measured at JKEO and KEO (Fig. 2) is generally large on daily to synoptic time scales. During Period I, the LHF can be as large as 500 W m^{-2} at the end of February and the beginning of March both at JKEO and at KEO (Fig. 2 (a)). The LHF shows notably rapid increases in these events. For the rest of Period I, the period without the thick lines in Fig. 2 (a) and (b), the average LHF at JKEO was 155.1 W m^{-2} and that at KEO was 240.8 W m^{-2} , with fluctuations at shorter time scales at the two sites that do not appear to be correlated with each other. The sequence of the SHF had a larger amplitude at JKEO (Fig. 2 (b)). There are also notable increases in SHF, which were coincident with the increases in LHF.

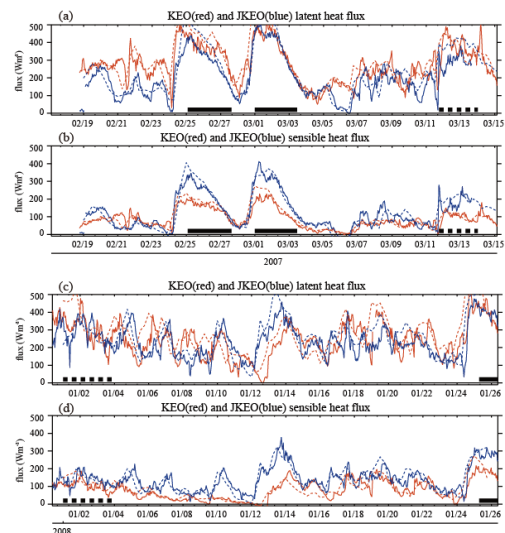


Figure 2: The latent and the sensible heat fluxes measured at KEO and JKEO are plotted by red and blue lines, respectively. Panels (a) and (b) show time sequences of hourly averaged latent heat flux and sensible heat flux obtained from the record every 10 minutes. The values of the JCDAS product at the collocated grid are superimposed by broken lines.

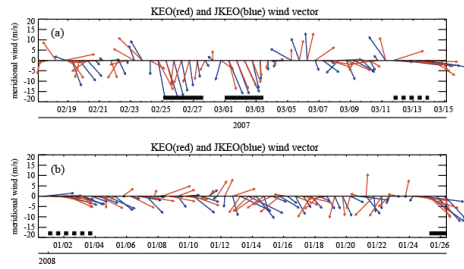


Figure 3: The vector wind diagram measured at KEO (red arrows) and JKEO (blue arrows) plotted during (a) Period I and (b) during Period II. The vertical axis indicates the meridional component of the wind vector, while the horizontal axis indicates the zonal component of the vector follows the vertical scale.

During Period II, the LHF occasionally exceeds 400 W m^{-2} , and the LHF and SHF at each buoy also seem to be closely correlated with each other (Fig. 2 (c) and (d)). The spatial difference of more than 100 W m^{-2} was observed several times associated with the maximum peak of the SHF and the LHF. There was stronger high frequency variability that was less coherent between the sites during Period II.

Bond and Cronin (2008) showed that the very large LHF and SHF events were associated with SLP pattern in which winds at KEO were anomalously northerly. In Fig. 3 we show the time sequence of the wind vector measured at KEO and JKEO. It is obvious in panel (a) that both SHF and LHF were maximized almost simultaneously during the strong northerly beginning on 24 and 28 February. From 11 March, the wind was almost westerly associated with the Siberian outbreak. During Period II, a simultaneous change between KEO and JKEO TBF was observed only at the end of the period. For other times, the THFs at KEO and JKEO seem to change independently, possibly due to short-term variation of the wind speed.

It is known that winter storms in the KE region are characterized by strong northerly wind. During these events, the TBF at the JKEO and KEO buoys increase almost simultaneously as shown in Fig. 2 and 3, although they are on opposite sides of the SST front. During other conditions, however, there are significant discrepancies between the two sites, even when the wind is strong.

It is expected that the spatial relationship between the SST front and the wind direction can affect the air mass transformation in the KE region and the TBF field. Therefore, we define two conditions correlated with the typical east Asian wintertime weather patterns, i.e., the northerly wind condition associated with the extraordinarily strong low pressure developing near the Kamchatka Peninsula, and the monsoon wind condition associated with the strong northwesterly of Siberian cold outbreak. Other times are characterized by frequent transitions in the weather pattern associated with the passage of highs and lows (Fig. 3), which do not cause so strong weather pattern. In particular, for this study, we identify the northerly wind condition as when the wind direction is within 30° from 180° (in the oceanographic convention) and the wind speed is over 8.0 m s^{-1} , and the monsoon wind condition as when the wind direction is within 30° from 110° and the wind speed is over 8.0 m s^{-1} . For a positive identification, these criteria must be satisfied for 60 % of the wind records in every 2 hours, and must last for more than a day at both KEO and JKEO.

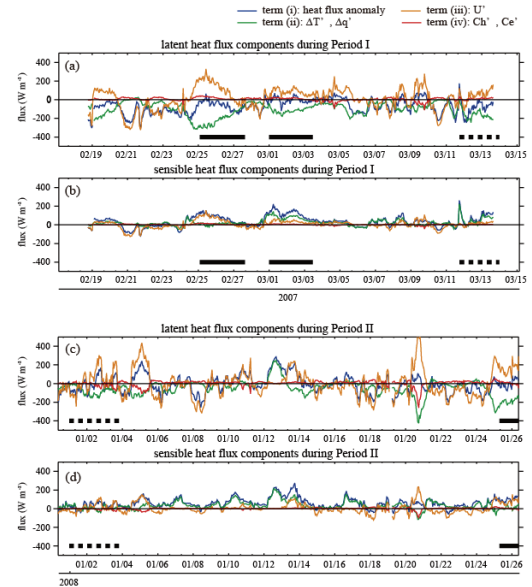


FIG. 4: Time series of the spatial anomaly components of the latent (panels (a) and (c)) and sensible (panels (b) and (d)) heat fluxes as indicated by eq. (1) and (2). Blue line shows the spatial anomaly of the heat flux expressed by term (i), green line the effect of the spatial anomaly of ocean-atmosphere gradient in temperature (ΔT) and humidity (Δq) expressed by term (ii), and orange line shows the effect of the wind anomaly expressed by term (iii). Red line shows the term (iv), the spatial anomaly of the bulk coefficients. Panels (a)-(b) are for Period I; panels (c)-(d) are for Period II, as in Fig. 3. Thick solid and broken lines indicate the period of the northerly wind condition.

In order to determine the factors responsible for causing the simultaneous heat flux differences at KEO and JKEO, we evaluate terms (ii), (iii) and (iv) in eq. (1) and (2). The sequences of individual terms in eq. (1) and (2) are shown in Fig. 4. The term (iv) is very small throughout the period, that indicates the spatial anomaly of bulk coefficients caused by those of boundary layer parameters is systematically compensated each other. On the other hand, the effect of the spatial anomaly of the air-sea gradient of specific humidity, Δq , ((ii) in eq. (2)) was almost balanced with that of the wind speed ((iii) in eq. (2)) during the northerly wind condition in Period I and Period II. This indicates that the wind speed in the downstream (KEO) was weaker than the upstream (JKEO), while Δq was enlarged in the downstream direction. The spatial difference in the SHF can be attributed to the wind speed difference, as the value of term (ii) is reduced. The wind speed difference can contribute to the spatial difference in the SHF. In these cases, although the air-sea temperature gradient ΔT on the north side of the SST front is almost the same as that on the south side, the humidity gradient Δq is larger on the south side of the front due to the nonlinearity in the Clausius-Clapeyron relation. This is the result of the air mass transformation as the cold air crosses the SST isotherms to restore to the warmer SST (Kondo, 1976; Nonaka et al., 2009).

Consequently, the LHF on each side of the KE front were simultaneously enhanced (Fig. 2), whereas the SHF in the northern side was larger under this weather condition. Recent numerical model studies demonstrated an increase of the air temperature on the strong SST front associated with the growth of the ABL and the water vapor contents along the cross frontal wind (Spall, 2007; Skillingstad and Edson, 2009).

During the monsoon wind condition, there is a distinct difference in the LHF and the SHF between KEO and JKEO. The LHF to the south of the KE front is larger than that to the north, whereas the SHF to the south is much less than that to the north. As one can see from the wind direction at KEO and JKEO, the strong monsoon winds, which blow almost parallel to the strong SST front of the KE, undergoes a different air mass transformation processes over the cold and warm ocean. It is noteworthy that the term (ii) in eq. (1) and that in eq. (2) seem to change independently (Fig. 4), whereas the wind speed and direction change almost simultaneously (Fig. 3).

As the air temperature is increased by the warm ocean surface south of the KE front, evaporation is enhanced due to the large Δq under the strong wind to the south of the KEO. In contrast, SHF north of the KE front is larger than the south. The sea surface cooling contrast across the KE front does not change so much, as the north-south differences of the SHF and the LHF tend to compensate each other.

For the rest of the period, the normal condition, the heat flux can be characterized by the generally larger evaporative cooling to the south of the KE front, and weaker SHF to the south on average during Period I. The contrast is relatively weak during Period II. The relationship between the TBF at KEO and JKEO is not systematic as it frequently changes almost on a daily time scale. It is true that the condition of TBF on the KE front is not analyzed by these buoys. The spatially gridded data such as the JCDAS is useful in spite of its low resolution in time and space.

These analyses suggest that the spatial pattern of the TBF in the KE region on monthly time scales is determined by the relative frequency of different types of wintertime weather conditions. In order to investigate this further, we conducted a composite analysis of the spatial pattern of the TBF using the reanalysis product of JCDAS. Composite maps of the TBF during northerly wind conditions, monsoon wind conditions, and normal conditions during Period I and II are shown in panels (a) to (c) in Figs. 5 and 6, as well as the overall average of the individual periods (panel (d)).

While the TBF is remarkably large in the center of the KE region, the spatial distributions of the TBF associated with differ-

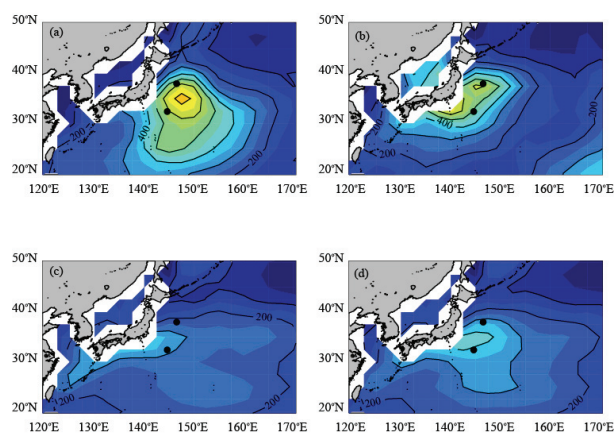


FIG. 5: Composites of the turbulent heat flux during (a) the northerly wind condition, (b) the NW monsoon wind condition, (c) the normal condition, and (d) the mean during Period I, obtained from the JCDAS product. Unit is in $W m^{-2}$. The position of KEO and JKEO are plotted by black circles.

ent weather patterns are quite distinct. As indicated in Fig. 5 (a) and Fig. 6 (a), during northerly wind conditions, the maximum value at the center of the KE is over $600 W m^{-2}$ on the frontal zone and large values over $400 W m^{-2}$ extend meridionally on both sides of the KE. On the other hand, during monsoon wind conditions, when the cold outbreak blows off of Siberia, the maximum heat flux is confined to a narrow band along the Kuroshio and the western portion of the KE front (Fig. 5 (b) and Fig. 6 (b)). The TBF in the KE region is generally smaller than during northerly wind conditions. Furthermore, during the monsoon conditions, the meridional change of the total TBF across the KE front is large.

The spatial composite of the TBF of the normal condition should be a reasonable one. The maximum heat flux is seen along the Kuroshio and KE because of the large ΔT and Δq , which is the result of the cold atmosphere over the warm ocean in this season. In monthly scale, average of the TBF shown in panels (d) in Fig. 5 and Fig. 6 to some extent reflects this condition by average. However, it significantly differs in magnitude and in the place of the maximum value from the normal condition.

The relative frequency of occurrence of the northerly wind and the monsoon wind condition could be partially responsible for the significant discrepancy between the TBF during Period I and Period II as shown in Fig. 5 (d) and Fig. 6 (d). Fig. 2 clearly shows that the northerly wind condition occurs more in Period I than in Period II and that the northerly wind condition was rather short in Period II. Furthermore, the monsoon wind condition was very strong in the beginning of Period II, which may affect the monthly scale average. In this way, the relative occurrence of the different types of weather conditions perhaps would strongly influence on the anomalously dominating heat flux spatial structure for a given period.

4. THE MEASUREMENT OF THE AIR-MASS TRANSFORMATION BY AMSR-E

The air-mass transformation process described in the previous section is made without any information about the atmospheric properties over the KE front. The atmospheric properties measured by AMSR-E and the instantaneous latent heat flux give the

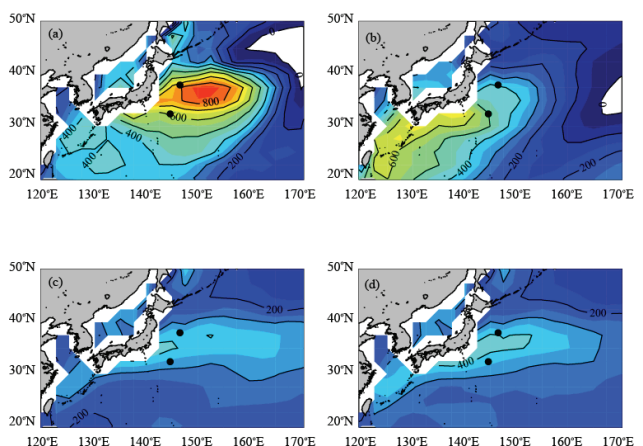


FIG. 6: Same as in Fig. 5, except for Period II.

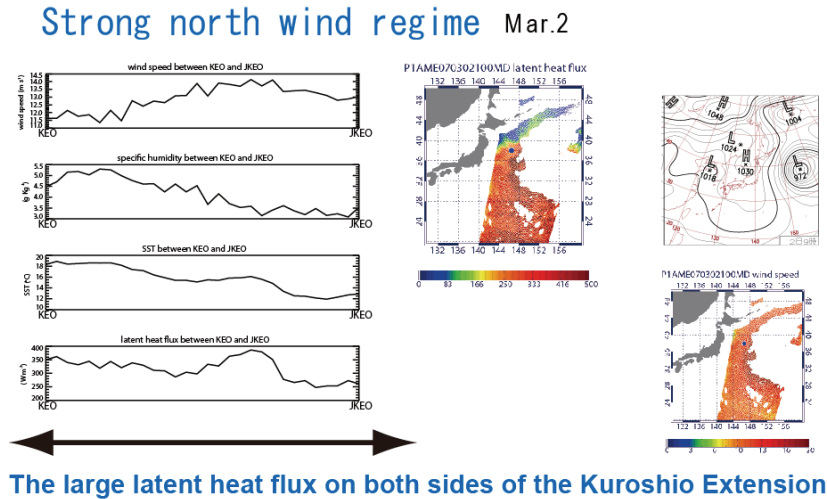


Fig.7 (a): The boundary layer parameters of the wind speed, specific humidity, SST, and latent heat flux between the KEO and the JKEO (right panel), and the map of the latent heat flux (center), and the weather chart with the wind speed map (left) on March 2.

information over the KE front, which can not be obtained by in situ measurement such as the surface mooring. Fig. 7 demonstrates the spatial distribution of the LHF in the KE region on March 3 during the northerly wind condition and on March 15 during the monsoon wind condition.

The center of Fig. 7 (a) shows the map of the instantaneous latent heat flux derived by AMSR-E along the swath. The figure clearly shows that the quite large LHF expands to the north and the south of the KE front. The left column shows the wind speed, specific humidity, SST, and the LHF between JKEO and KEO. The figure shows that the wind speed near JKEO is stronger than that near KEO, as speculated previously. It is also supported by the weather chart and the map of the wind speed (right panel). The specific humidity to the northern side (JKEO) is very small. It is clearly seen that the atmosphere gradually becomes humid to the south. The resultant LHF is as large as 300 W m^{-2} both to the north and to the south of the SST front. The large LHF exists far from the KE front. The spatial change of these variables strongly supports our speculation about the air-mass transformation along the advection of the atmospheric

mass due to the strong northerly.

On the other hand, during the monsoon wind condition, the situation is quite different. The center panel of Fig. 7 (b) shows that the LHF to the north of the KE front is much larger than that to the south. The wind speed is not necessarily correlated with the SST. The large specific humidity is seen associated with the weak wind speed, rather than the SST front. This should indicate that the atmosphere undergoes the independent air-mass transformation in the different weather conditions across the KE front. As the result, the large LHF is confined within the nearby and the north of the front. The difference of the air-mass transformation between the northerly wind condition and the monsoon wind condition is confirmed by the simultaneous measurement of the boundary layer parameters and the LHF by AMSR-E. In this way, the combined use of the in situ and the remote sensing enables us to investigate the air-sea interaction process, which needs the boundary layer parameters with high resolution.

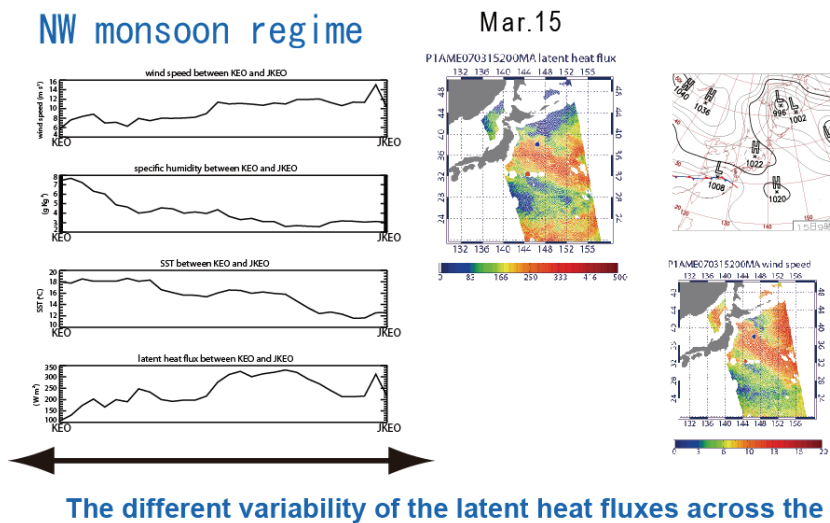


Fig. 7 (b) continued: same as panel (a) except for the data on March 15.

5. SUMMARY

We analyzed the winter surface heat flux variability and its difference between the north (JKEO) and the south (KEO) sides of the KE front in daily to synoptic timescales. The KEO buoy station has been located in the Kuroshio recirculation gyre south of the KE jet since June 2004. Measurement at the JKEO station, in the Mixed Water Region north of the KE, began in February 2007. In this study we consider two winter periods of coincident observations at KEO and JKEO; Period I: 18 February 2007 to 12 March 2007 and Period II: 1 to 25 January 2008.

In wintertime, the SHF and the LHF were quite large both at KEO and JKEO. It was found that the LHF eventually exceeds 400 W m^{-2} , while the SHF is also as large as 200 to 300 W m^{-2} . We found that these extreme conditions are produced in close relation with the speed and direction of the prevailing wind.

The northerly wind condition is characterized by cross-frontal northerly wind and extraordinarily large TBF, both to the north and south of the KE front. As a result of the air mass transformation along the prevailing wind, the large air-sea gradient in humidity (Δq) over the warm ocean south of the KE front can enhance the evaporative cooling, whereas the wind is stronger to the north. As a consequence LHF has little contrast across the KE front, although SHF in the north is larger than to the south due to the stronger wind north of the front.

The monsoon wind condition is also characterized by strong northwesterly wind and large heat flux in the KE region. However, the spatial difference of the LHF and SHF did not seem to be systematic. The LHF to the north of the KE front was significantly smaller than that to the south because of the nonlinearly increasing air-sea gradient of humidity. As the prevailing wind is almost parallel with the KE front, changes in the heat fluxes on the north and south sides of the KE front are not necessarily simultaneous.

During the normal condition, the maximum heat flux tends to be confined along the KE jet, and is generally smaller than the turbulent fluxes found during the other two weather patterns. This condition possibly reflects the typical environment in the KE region with the cold atmosphere over the warm current.

The spatial structures of the THF due to different weather conditions proposed in this study highlights the basic fact that THF and atmospheric modification strongly depend on lateral advection that occurs during weather events. One of the important findings in this study is that the TBF on near-monthly time scales and its spatial distribution are closely related to the relative frequency of synoptic events. This result accentuates the importance of the high-frequency monitoring of the thermal air-sea interaction in the KE region.

An advantage of surface buoy measurements is that they highly resolve temporal variations. Their disadvantage is that they generally undersample the spatial structure. For this, numerical model products and satellite measurements are better suited. As demonstrated in this analysis, however, the spatial structure depends upon capturing the synoptic temporal variability accurately, making the KEO and JKEO reference stations particularly valuable for validating these products (Konda et al., 2009).

The surface meteorological and oceanic data at KEO used in this study were provided by NOAA / PMEL. The data of JKEO were obtained from JAMSTEC / Research Institute for Global Change. The reanalysis dataset used for this study are provided from the cooperative research project of the JRA-25 long-term reanalysis by Japan Meteorological Agency and Central Research Institute of Electric Power Industry. Level 1B brightness temperature and Level 2 geophysical parameters of AMSR-E are provided by Earth Observation Research and Application Center, JAXA. This study is supported by the Joint Research Program between Kyoto University and JAXA "Evaluation of the sea surface flux through the improvement of the wind speed derived by GCOM-W1 AMSR2".

REFERENCES

- Bond, N. A. and M. F. Cronin, 2008. Regional weather patterns during anomalous air-sea fluxes at the Kuroshio Extension Observatory (KEO). *J. Climate*, 21, pp. 1680-1697.
- Cronin, M. F., C. Meinig, C. L. Sabine, H. Ichikawa, and H. Tomita, 2008. Surface mooring network in the Kuroshio Extension. *IEEE Systems J.*, 2, pp. 424-430.
- Fairall, C. W., E. F. Bradley, J. E. Hare, A. A. Grachev, and J. B. Edson, 2003. Bulk parameterization of air-sea fluxes: Updates and verification for the COARE algorithm. *J. Climate*, 16, pp. 571-591.
- Kalnay, E., and Coauthors, 1996. The NCEP/NCAR 40-Year Reanalysis Project. *Bull. Amer. Meteor. Soc.*, 77, 437-470.
- Konda, M., A. Shibata, N. Ebuchi, K. Arai, 2006. A correction of the effect of relative wind direction on the wind speed derived by Advanced Microwave Scanning Radiometer. *J. Oceanogr.*, 62, pp. 395-404.
- Konda, M., H. Ichikawa, H. Tomita 2009. Wind speed and latent heat flux retrieved by simultaneous observation of multiple geophysical parameters by AMSR-E. *J. Remote Sens. Soc. Japan*, 29, pp. 191 - 198.
- Kondo, J. 1976. Heat balance of the East China Sea during the Air Mass Transformation Experiment. *J. Meteor. Soc. Japan*, 54, pp. 382-398.
- Kubota, M., A. Kano, H. Muramatsu, and H. Tomita, 2003. Intercomparison of various surface latent heat flux fields. *J. Climate*, pp. 16, 670-678.
- Nakamura H., T. Sampe, A. Goto, W. Ohfuchi, and S.-P. Xie, 2008. On the importance of mid-latitude oceanic frontal zones for the mean state and dominant variability in the tropospheric circulation. *Geophys. Res. Lett.*, 35, L10079, doi:10.1029/2008GL034010.
- Nonaka, M, H. Nakamura, B. Taguchi, N. Komori, A. Kuwano-Yoshida, and K. Takaya, 2009. Air-sea heat exchanges characteristic to a prominent midlatitude oceanic front in the South Indian Ocean as simulated in a high-resolution coupled GCM. *J. Climate*, 22, pp. 6515-6535.
- Onogi, K., and Coauthors, 2007. The JRA-25 reanalysis. *J. Meteor. Soc. Japan*, 85, 369-432.
- Qiu, B., S. Chen, and P. Hacker, 2004. Synoptic-scale air-sea flux forcing in the western North Pacific: Observations and their impact on SST and the mixed layer. *J. Phys. Oceanogr.*, 34, 2148-2159.
- Skyllingstad, E. D., and J. B. Edson, 2009. Large-Eddy Simulation of moist convection during a cold air outbreak over the Gulf Stream. *J. Atm. Sci.*, 66, 1274-1293.
- Spall, M. A., 2007. Midlatitude wind stress-Sea surface temperature coupling in the vicinity of oceanic fronts. *J. Climate*, 20, 3785-3801.

ACKNOWLEDGEMENTS